Scripta Materialia 169 (2019) 82–86

Contents lists available at ScienceDirect

Scripta Materialia

journal homepage: www.elsevier.com/locate/scriptamat

Synchrotron X-ray Laue diffraction study of hydrogen-induced blisters on iron grain boundaries

Xuan Tao [a,b], Guo-Cai Lv [a], Jiawei Kou [c], Xilin Xiong [a,b], Alex A. Volinsky [d], Ching-Shun Ku [e], Kai Chen [c,*], Yan-Jing Su [a,b,**]

[a] Beijing Advanced Innovation Center for Materials Genome Engineering, University of Science and Technology Beijing, Beijing 100083, PR China
[b] Corrosion and Protection Center, Key Laboratory for Environmental Fracture (MOE), University of Science and Technology Beijing, Beijing 100083, PR China
[c] Center for Advancing Materials Performance from the Nanoscale (CAMP-Nano), State Key Laboratory for Mechanical Behavior of Materials, Xi'an Jiaotong University, Xi'an, Shaanxi 710049, PR China
[d] Department of Mechanical Engineering, University of South Florida, Tampa 33620, USA
[e] National Synchrotron Radiation Research Center, Hsinchu 300, Taiwan, ROC

ARTICLE INFO

Article history:
Received 10 January 2019
Received in revised form 7 May 2019
Accepted 9 May 2019
Available online xxxx

Keywords:
Grain boundaries
Iron
Hydrogen blister
Synchrotron X-ray Laue nano-diffraction

ABSTRACT

The effects of grain boundaries (GBs) on the initiation of hydrogen-induced blisters in pure iron were investigated using synchrotron polychromatic X-ray Laue nano-diffraction. It was found that the random GBs were more susceptible to blistering than the coincidence site lattice grain boundaries. High strain levels and severe plastic deformation were observed around the random GBs after hydrogen charging, but not on the coincidence site lattice grain boundaries.

Ever since Johnson's first report on hydrogen embrittlement (HE) in 1874 [1], numerous efforts have been undertaken to study this group of deleterious phenomena. Hydrogen atoms trapped at defects would recombine with each other into molecules, forming the nucleus of the blisters and increasing local pressure, thus facilitating internal cracks and blisters [2], which shorten the fatigue life of metallic materials [3].

The hydrogen-induced pressure, which makes the cracks propagate discontinuously, can now be measured [4]. So far much work has focused on the blisters observed around inclusions [4–9]. Grain boundaries (GBs), as the most prevailing traps of hydrogen in polycrystalline materials, also play an essential role in the formation of blisters [10]. Tritium radioluminography has confirmed that hydrogen atoms preferred to segregate at GBs in Al and Mo [11,12]. Also, in pure iron, hydrogen-induced cavities and pores, which are the nuclei of the blisters, were observed along GBs [13]. Moreover, experimental and theoretical evidence was provided demonstrating that small hydrogen blisters were formed at GBs in W [14,15]. Considerable efforts have revealed the differences between coincident site lattice (CSL) GBs and random GBs in hydrogen diffusion and trapping [16–18], as well as hydrogen-induced cracking initiation and propagation [19,20]. There is no doubt that the structure of GB plays a crucial role in HE sensitivity [21–23]. Hence, the nature of the GBs, especially on the sample surface, should have a significant impact on the formation of blisters. However, a systematic study of this effect is still lacking.

Traditional materials characterization techniques, such as electron backscatter diffraction (EBSD) and transmission electron microscopy (TEM), require sophisticated sample preparation, which may destroy the blisters or introduce artificial defects. Therefore, the relationship between hydrogen blisters and GBs is challenging to uncover. Nevertheless, with the help of micro- or even nano-focused high-brilliance X-ray beams produced in modern synchrotron facilities, polychromatic X-ray Laue nano-diffraction (XND) can resolve this challenge [24,25]. When the polychromatic X-ray beam with continuous spectrum in a relatively wide range of wavelengths impinges on an individual crystalline grain, the Bragg condition will be satisfied on various crystalline planes simultaneously without rotating the sample, thus a Laue pattern can be collected using a two-dimensional (2D) detector in only one exposure [26]. To obtain adequate statistics, usually an area on the specimen surface will be raster scanned, and at each scanning position, a Laue pattern will be collected. By analyzing all the Laue patterns, the spatial distribution of phases [25], crystal orientations [27], GBs [28], elastic [29] and plastic deformation can be mapped [30]. Compared

* Corresponding author.
** Correspondence to: Y.-J. Su, Beijing Advanced Innovation Center for Materials Genome Engineering, University of Science and Technology Beijing, Beijing 100083, PR China.
E-mail addresses: volinsky@usf.edu (A.A. Volinsky), kchenlbl@gmail.com (K. Chen), yjsu@ustb.edu.cn (Y.-J. Su).

https://doi.org/10.1016/j.scriptamat.2019.05.009
1359-6462/

with EBSD, XND provides better angular (below 0.01°) and lattice strain (below 10^{-4}) resolution. Moreover, XND does not require complicated sample surface preparation due to the high penetration depth of X-rays [31]. In this paper, the effects of GBs on blister initiation in pure iron are explored utilizing the XND technique, with the purpose to study the GB effects on the initiation of hydrogen blisters.

99.9% pure iron was used in this study. As-received samples were first fully annealed in vacuum at 1200 °C for 2 h, and then machined into small pieces with the $8 \times 6 \times 1$ mm^3 dimensions for hydrogen charging. Majority of the grain diameters fell in the 100–200 μm range. All the samples were electrochemically charged using the galvanostatic method in a solution of 0.5 mol/L H_2SO_4 with 0.22 g/L thiourea acting as hydrogen promoter. To investigate the morphology and spatial distribution of the blisters, the hydrogen charging parameters of current density and charging time were varied in the range of 5 to 50 mA/cm^2 and 10 min to 24 h, respectively.

The XND experiments were carried out at the Beamline 21A of the Taiwan Photon Source, National Synchrotron Radiation Research Center. The X-ray beam size was focused to ~100×100 nm^2 by using a pair of orthogonal ultra-smooth mirrors shaped into ellipses in the Kirkpatrick-Baez configuration. Samples were mounted on an *x-y* scanning stage with an inclination angle of 45° with respect to the incident polychromatic X-ray beam with the energy range of 5 to 30 keV. The samples and the *x-y* scanning stage are integrated into a scanning electron microscope (SEM), which is equipped with a secondary electron detector, and thus the sample morphology can be observed and the X-ray scanning area can be conveniently determined. In this report, H-charged and uncharged samples were tested with the 8 μm scanned step size and the 0.5 s exposure time. At each scanning step, a Laue pattern was collected using the in-vacuum Pilatus 3S-6M detector, which was placed above the sample at a distance of about 520 mm. The accurate diffraction geometry was calibrated by using a Laue pattern from a strain-free Si single crystal, which was positioned right beside the pure iron specimen. All the Laue patterns were analyzed automatically using the custom-developed software package XMAS [32], taking advantage of the newly developed peak position comparison (PPC) indexing algorithm [33].

Fig. 1 shows the morphology and location of the blisters under different charging conditions. Blisters of different sizes were generated simultaneously when the sample was charged for a long period of time. Blisters smaller than 20 μm, which is approximately the smallest grain size in all samples, were defined as small blisters, and large blisters referred to the ones that were larger than 20 μm. As seen in Fig. 1(a), larger blisters, with mostly an oval shape, often extend across 2 or 3 triple junctions (TJs). In the meantime, small blisters, marked by black arrows in Fig. 1(b), mainly sit right on the GBs. When subjected to high current density, the shape of the blisters became more irregular, and the "blister on blister" phenomenon was observed, as clearly displayed by arrows in Fig. 1(c). Intriguingly, on cap tiny blisters were often found on GBs of the large blister caps. A typical example is presented in Fig. 1(d), where the already broken small blister lies right across the GB.

It was found that the charging time and current density mainly altered the size and shape, but not the locations of the blisters. In all the tested conditions, the spatial distribution of the blisters, especially the small ones, showed a common preference towards GBs, indicating potential initiation preference of blisters to form around GBs, which is

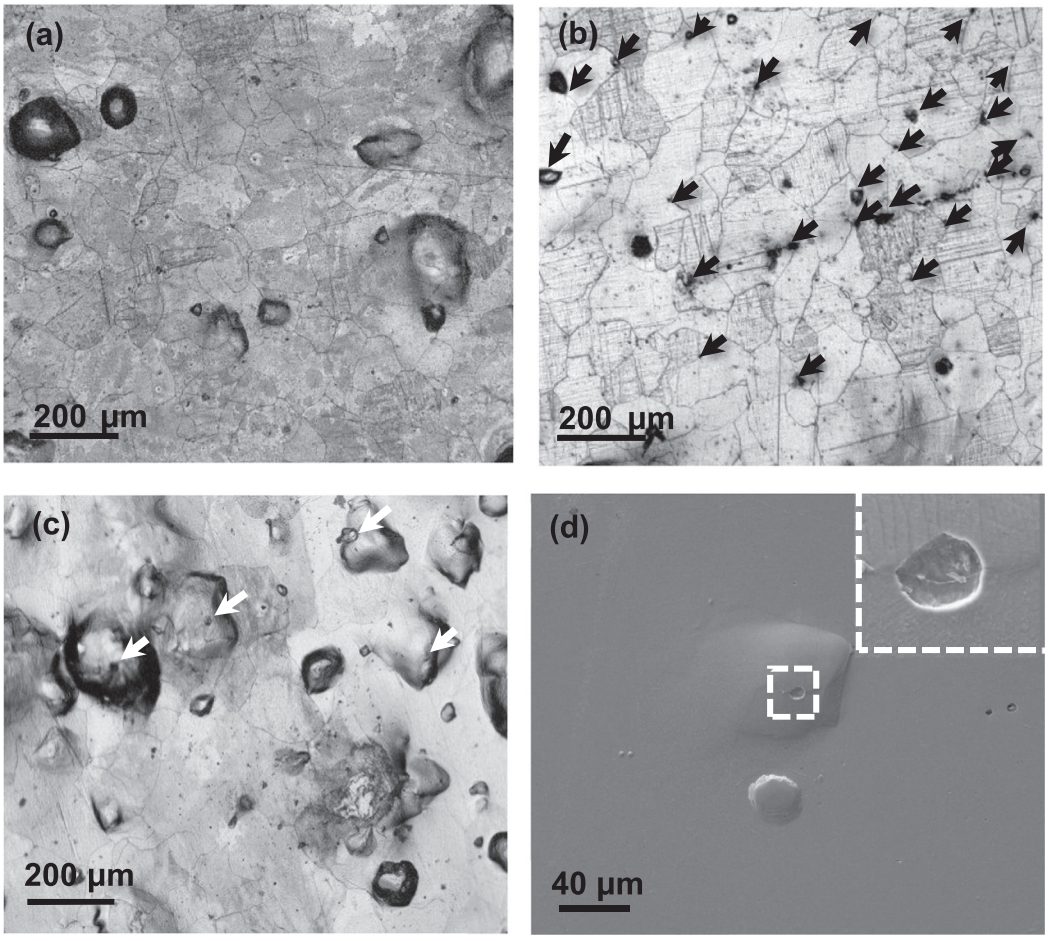

Fig. 1. Optical micrographs of 10 mA/cm^2, 12 h charged sample: (a) Large blisters with mostly regular, oval shapes; (b) small blisters with arrows marking the ones right on GBs; (c) optical micrograph of 50 mA/cm^2, 6 h charged sample. GB "blister on blister" phenomena are marked by arrows; (d) SEM images of blister lying right on the GB on blister cap.

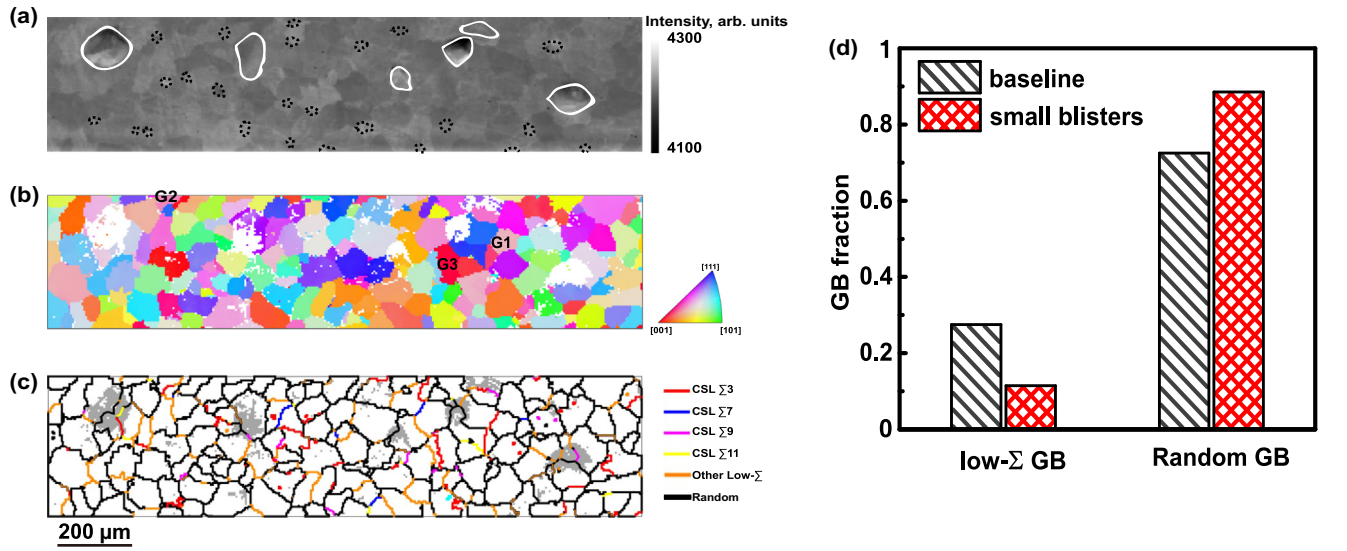

Fig. 2. (a) X-ray intensity map of the tested region obtained from X-ray nano-diffraction data processed by the XMAS software and the PPC method; (b) IPF-Z map of the detected region; (c) CSL GB mapping of the detected region; (d) statistical analysis of GBs and blisters: ratio of GB types that generate small blisters (red) compared with their occurrence in the baseline microstructure (grey). (For interpretation of the references to color in this figure legend, the reader is referred to the web version of this article.)

consistent with other findings [5,34–37]. Blister location proportion for different charging conditions was calculated based on the hydrogen charging results. It was found that nearly 2/3 of the small blisters were generated right on a single GB, while about 3/4 of the large blisters tended to occupy TJs. GBs act as primary defects in pure materials, providing favorable sites for blisters initiation [12], thus explaining the preference of blisters growth on GBs.

The sample used in the XND experiment was charged with hydrogen at a constant current density of 50 mA/cm^2 for 1 h. An area of 2540 $\times$ 600 μm^2 was scanned. About 30 hydrogen blisters were found in the scanned area, five of which were large enough to be visible with the naked eye. It has been demonstrated that the topology of the sample surface can be visualized by plotting the average intensity distribution of each 2D Laue pattern [24]. In the average intensity map in Fig. 2(a), large and small blisters are outlined by white and black colors, respectively. Inverse pole figure normal to the sample surface (IPF-Z) is shown in Fig. 2(b), and no obvious orientation preference of the blister initiation was found.

To investigate the effects of GB types on blister initiation, statistical analysis was conducted. One thing to be noticed: in the detected area, the large blisters were too large to identify the initiation process, since their size was equivalent to or larger than the grains. Additionally, only six large blisters were observed, making the sample size too small to draw any statistically significant conclusions. Small blisters, on the other hand, are suitable for predicting blister initiation. Therefore, only small blisters were used in the statistical calculation procedure.

CSL GBs were defined by the coincidence theory [38], using the Brandon criterion [39]. GBs with $\Sigma \leq 29$ are considered to be the low-Σ GBs [17,20]. Identification of the GB types was performed with the MTEX software in Matlab 2016b, using the data collected by the XND scan. CSL GBs are marked in different colors and random GBs are black, as shown in Fig. 2(c). All GBs in the scanned area were recorded as N, and the ratios of the low-Σ GBs and random GBs were calculated according to Table 1, where $N_{\text{low-}\Sigma}$ and N_{random} are the numbers of the low-Σ and random GBs, respectively. These two ratios serve as the frequency baseline of these two types of GBs in the entire sample. The fractions of several specific types of the low-Σ GBs were also calculated. It was found that the fraction of Σ3 GB in the tested area is about 6%, while Σ7 GB is ~1%, Σ9 GB and Σ11 GB each takes up 5%, and all other low-Σ GBs occupy a total of 15% with the balanced distribution. Although some types of GBs exhibit a slightly higher fraction, it is still within a comparable distribution range. Meanwhile, GBs with small blisters were recorded as N_{small}, and among them the number of low-Σ ($N^{small}_{low-\Sigma}$) and random GBs (N^{small}_{random}) were identified and the corresponding ratios were calculated.

Fig. 2(d) shows a statistical analysis of the GB types and small blisters. 61 GBs that were found with 25 small blisters were taken into consideration. 7 out of the 61 (~11%) GBs are low-Σ GBs. This value was actually lower than the frequency of low-Σ GBs in the entire sample. Meanwhile, 54 of them were random GBs, reaching a fraction of 89%, suggesting that random GBs are more prone to generating blisters. To further confirm this observation, the p-value, which is useful in telling whether a hypothetical trend is reasonable, was calculated based on the acquired data [20]. The null hypothesis was that all the GBs shared the same tendency to initiate hydrogen blisters. The alternative hypothesis was that blisters were less likely to initiate on low-Σ GBs, while they were more likely to initiate on random GBs.

From the number of small blisters on GBs, we calculated the p-values for the two kinds of GBs and obtained the p-value of 0.006, which is much lower than $\alpha = 0.05$, indicating that the null hypothesis can be rejected. This means that the hydrogen blisters were more likely to initiate on random GBs.

The dislocation type and density in the local sample volume illuminated by the focused X-ray beam can be determined from the shape of the Laue peaks, and thus the plastic deformation can be interpreted [40]. Sharp Laue peaks indicate no or low dislocation density, while high dislocation density broadens the Laue peaks. If this broadening is isotropic, statistically stored dislocations (SSDs) are dominant in the

Table 1
Ratio calculation of low-Σ and random GBs in the baseline structure or generated small blisters.

N	$N_{\text{low-}\Sigma}$	N_{random}	N_{small}	$N^{small}_{\text{low-}\Sigma}$	N^{small}_{random}
672	185	487	61	7	54
Baseline structure ratio	0.275	0.725	Small blisters ratio	0.114	0.886

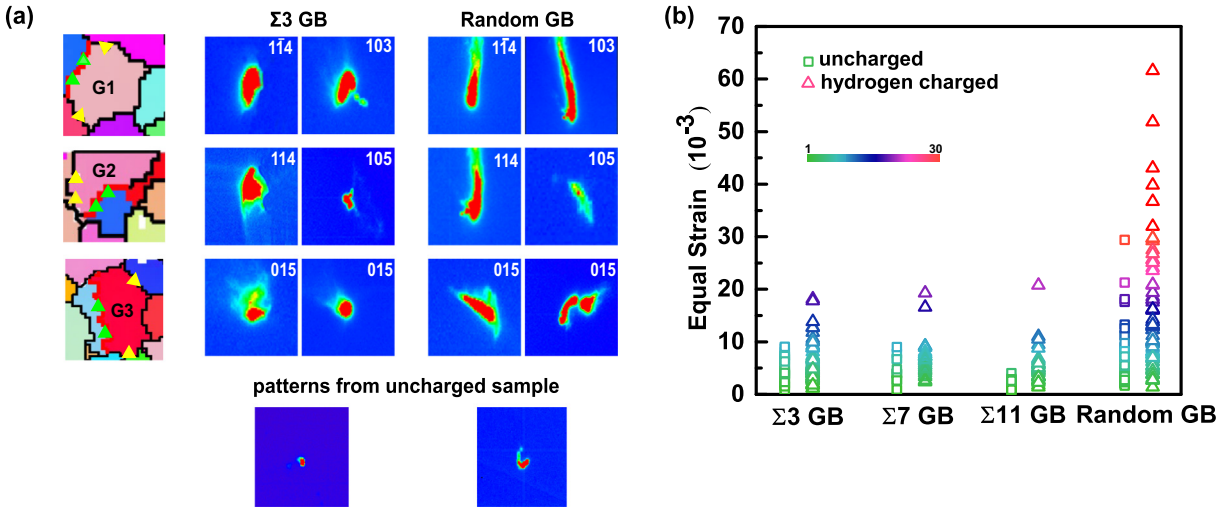

Fig. 3. (a) Magnified pattern on different GBs. Patterns of Σ3 GB are represented by green triangles and random GB are represented by yellow triangles. Patterns from uncharged GBs are shown for reference; (b) strain distribution on different GB types in uncharged and 1 h charged samples. (For interpretation of the references to color in this figure legend, the reader is referred to the web version of this article.)

corresponding volume of the specimen. Geometrically necessary dislocations (GNDs), on the other hand, cause anisotropic broadening of the Laue peaks, which is usually called streaking [41,42]. The streaking direction depends on the slip system of the GNDs and the orientation of the crystalline grain [43]. In both SSD and GND dominant cases, the dislocation density can be quantitatively estimated from the peak width [41,43].

To investigate the deformation caused by hydrogen charging on different types of GBs, three grains, marked as G1, G2, and G3 in Fig. 2(b), were selected for the study. Each of these grains contained both random and Σ3 GBs, and no large blisters were detected on them. On both the random and Σ3 GBs of each grain, two positions were examined in detail, respectively. All the spots were indexed with two sets of peaks, indicating that these spots were located at the very vicinity of GBs. The same reflections from the mutually indexed grains were studied. Enlarged images of the spots and reflections are shown in Fig. 3(a). Patterns taken from Σ3 GB and random GB on another sample, which was not charged with hydrogen, are also presented for comparison.

It can be observed that all the Laue diffraction patterns from the uncharged sample from the two kinds of GBs are sharp, while Laue patterns from the hydrogen-charged sample exhibit significant broadening, suggesting hydrogen-induced deformation on both kinds of GBs. Furthermore, Σ3 GBs show a relatively smaller deformation level than random GBs. This difference becomes obvious after hydrogen charging, as seen in Fig. 3(a). Laue spots of the three grains exhibit the same trend: reflections on Σ3 GBs are relatively sharp, whereas the patterns on random GBs are streaking. Any deformation found on Σ3 GBs (reflections $1\bar{1}4$, 103 in G1, 114 in G2) is minor compared with the significant deformation of random GBs. Additionally, in the case of the 105 peak in G3, both streaking and splitting are observed. Based on these results, it can be concluded that random GBs endured more plastic deformation than Σ3 GBs. Note that no evident blisters were detected in all investigated spots, indicating that the localized plasticity around random GBs did not result from the growth of the blisters. Although there might be undetectable blister nuclei in the scanned area that could induce deformation, this still indicated that the localized plasticity around random GBs played a role in the blisters initiation process.

Equal von Mises strains of four kinds of GBs before and after hydrogen charging are plotted in Fig. 3(b). Random GBs originally exhibited higher strain level. After hydrogen charging, the strain level of all four

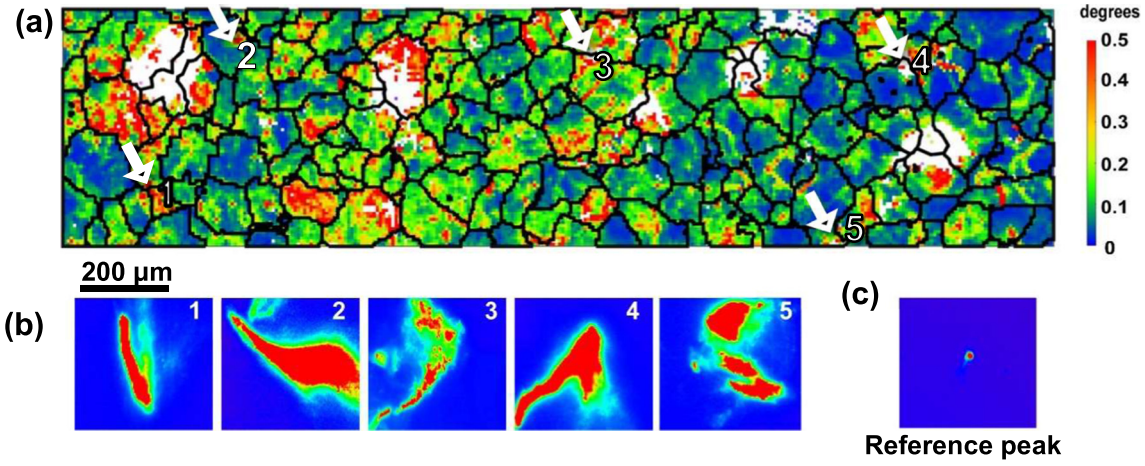

Fig. 4. (a) Local misorientation distribution obtained from indexed data; (b) magnified nano-diffraction peaks from the marked areas in (a); (c) reference pattern from the uncharged sample.

kinds of GBs increased. Furthermore, the strain level of random GBs increased dramatically compared with low-Σ GBs. This observation demonstrated that plastic deformation localized around random GBs. Elevated strain levels on random GBs are closely related to their more open structure compared to the CSL ones. Vacancy-like free volume structure and large excess volume [5] in random GBs generated gaps between bulk and GBs, providing local high vacancy concentration and a certain volume, which are the necessities for hydrogen atoms to recombine into molecules [2]. Once the molecules are formed, local pressure level rises, causing localized deformation, generating stress field around GBs, thus resulting in the stress-induced hydrogen diffusion [44], bringing more hydrogen atoms for the blister nucleus to grow. Thus, random GBs were found with more hydrogen blisters.

The degree of plastic deformation induced by hydrogen charging and blister formation can be approximated from the crystal misorientation distribution map obtained from the XND study (Fig. 4). Misorientations around blisters are obviously higher than in other areas. Reflections taken from random GBs, which formed small blisters, are marked by white arrows in Fig. 4(a), and demonstrated in Fig. 4(b). It is clear that plastic deformation around the small blisters is more severe than in the area where no blisters were generated. Remarkable streaking and splitting were observed, and the streaking points extended in different directions, suggesting that more than one slip systems were activated [30,40].

In conclusion, the effects of GBs on the initiation of blisters in pure iron were explored using synchrotron X-ray Laue nano-diffraction. It was found that hydrogen blisters preferred to form on random GBs rather than on low-Σ GBs. Results also showed that random GBs exhibited higher strain levels and more severe plastic deformation than low-Σ GBs after hydrogen charging. Moreover, this study proved that the Laue nano-diffraction can be utilized to measure minute local strain changes associated with hydrogen charging.

Acknowledgments

This work is supported by the National Natural Science Foundation of China (51571028 and 51671154), the Discipline Innovative Engineering Plan of China (111 Project, B17003). A.A.V. acknowledges support from the National Science Foundation (IRES 1358088). C.S.K. acknowledges support from the MOST Taiwan (106-2119-M-213-001-MY3). We appreciate technical support from Dr. S.J. Chiu, C.Y. Chiang, and C.H. Lin (National Synchrotron Radiation Research Center) for the XND experiments.

References

[1] W.H. Johnson, Proc. R. Soc. Lond. 23 (156–163) (1874) 168–179.
[2] W. Geng, L. Wan, J.-P. Du, A. Ishii, N. Ishikawa, H. Kimizuka, S. Ogata, Scr. Mater. 134 (2017) 105–109.
[3] J.B. Condon, T. Schober, J. Nucl. Mater. 207 (1993) 1–24.
[4] M.C. Tiegel, M.L. Martin, A.K. Lehmberg, M. Deutges, C. Borchers, R. Kirchheim, Acta Mater. 115 (2016) 24–34.
[5] X.C. Ren, Q.J. Zhou, G.B. Shan, W.Y. Chu, J.X. Li, Y.J. Su, L.J. Qiao, Metall. Mater. Trans. A 39 (1) (2008) 87–97.
[6] X. Ren, W. Chu, J. Li, Y. Su, L. Qiao, Mater. Chem. Phys. 107 (2) (2008) 231–235.
[7] B.E. Widle, C.D. Kim, E.H. Phelps, Corrosion. 36 (11) (1980) 625–632.
[8] C.F. Dong, X.G. Li, Z.Y. Liu, Y.R. Zhang, J. Alloys Compd. 484 (1) (2009) 966–972.
[9] X.S. Du, W.B. Cao, C.D. Wang, S.J. Li, J.Y. Zhao, Y.F. Sun, Mater. Sci. Eng. A 642 (2015) 181–186.
[10] G. Pressouyre, Metall. Mater. Trans. A 14 (10) (1983) 2189–2193.
[11] T. Hoshihira, T. Otsuka, T. Tanabe, J. Nucl. Mater. 390 (2009) 1029–1031.
[12] T. Hoshihira, T. Otsuka, T. Tanabe, J. Nucl. Mater. 386 (2009) 776–779.
[13] A. Griesche, E. Dabah, T. Kannengiesser, N. Kardjilov, A. Hilger, I. Manke, Acta Mater. 78 (2014) 14–22.
[14] Y. Ueda, T. Funabiki, T. Shimada, K. Fukumoto, H. Kurishita, M. Nishikawa, J. Nucl. Mater. 337 (2005) 1010–1014.
[15] H.-B. Zhou, Y.-L. Liu, S. Jin, Y. Zhang, G.-N. Luo, G.-H. Lu, Nucl. Fusion 50 (2) (2010), 025016.
[16] A. Oudriss, S. Le Guernic, Z. Wang, B. Osman Hoch, J. Bouhattate, E. Conforto, Z. Zhu, D.S. Li, X. Feaugas, Mater. Lett. 165 (2016) 217–222.
[17] A. Oudriss, J. Creus, J. Bouhattate, E. Conforto, C. Berziou, C. Savall, X. Feaugas, Acta Mater. 60 (19) (2012) 6814–6828.
[18] Z. Ma, X. Xiong, L. Zhang, Z. Zhang, Y. Yan, Y. Su, Electrochem. Commun. 92 (2018) 24–28.
[19] T. Watanabe, Mater. Sci. Eng. A 176 (1–2) (1994) 39–49.
[20] M. Seita, J.P. Hanson, S. Gradečak, M.J. Demkowicz, Nat. Commun. 6 (2015) 6164.
[21] K.N. Solanki, M.A. Tschopp, M.A. Bhatia, N.R. Rhodes, Metall. Mater. Trans. A 44 (3) (2013) 1365–1375.
[22] I. Adlakha, K. Solanki, Acta Mater. 118 (2016) 64–76.
[23] S. Bechtle, M. Kumar, B.P. Somerday, M.E. Launey, R.O. Ritchie, Acta Mater. 57 (14) (2009) 4148–4157.
[24] G. Zhou, W. Zhu, H. Shen, Y. Li, A. Zhang, T. Nobumichi, K. Chen, Sci. Rep. 6 (2016), 28144.
[25] X. Chen, C. Dejoie, T. Jiang, C.S. Ku, N. Tamura, MRS Bull. 41 (6) (2016) 445–453.
[26] J. Chao, M.L.S. Fuller, N.S. Mcintyre, A.G. Carcea, R.C. Newman, M. Kunz, N. Tamura, Inc, 2012.
[27] H.R. Wenk, K. Chen, R. Smith, Am. Mineral. 96 (8–9) (2011) 1316–1324.
[28] Y. Li, D. Qian, J. Xue, J. Wan, A. Zhang, N. Tamura, Z. Song, K. Chen, Appl. Phys. Lett. 107 (18) (2015) 361–543.
[29] K. Chen, M. Kunz, N. Tamura, H.R. Wenk, Geo. 43 (3) (2015) 219–222.
[30] D. Qian, J. Xue, A. Zhang, Y. Li, N. Tamura, Z. Song, K. Chen, Sci. Rep. 7 (1) (2017) 2859.
[31] Y. Li, L. Wan, K. Chen, J. Appl. Crystallogr. 48 (2015) 747.
[32] B. Rozaliya, I. Gene, Strain and Dislocation Gradients From Diffraction: Spatially-resolved Local Structure and Defects, Imperial College Press, London, 2014.
[33] J. Kou, K. Chen, N. Tamura, Scr. Mater. 143 (2018) 49–53.
[34] A.H.M. Krom, A. Bakker, R.W.J. Koers, Int. J. Press. Vessel. Pip. 72 (2) (1997) 139–147.
[35] M. Van der Burg, E. van der Giessen, R. Brouwer, Acta Mater. 44 (2) (1996) 505–518.
[36] A. Laureys, E. Van den Eeckhout, R. Petrov, K. Verbeken, Acta Mater. 127 (2017) 192–202.
[37] D.P. Escobar, C. Miñambres, L. Duprez, K. Verbeken, M. Verhaege, Corros. Sci. 53 (10) (2011) 3166–3176.
[38] H. Grimmer, W.T. Bollmann, D. Warrington, Acta Crystallogr. Sect. A Cryst. Phys. Diffr. Theor. Gen. Crystallogr. 30 (2) (1974) 197–207.
[39] D. Brandon, Acta Metall. 14 (11) (1966) 1479–1484.
[40] M.P. Popovic, K. Chen, H. Shen, C.V. Stan, D.L. Olmsted, N. Tamura, M. Asta, M.D. Abad, P. Hosemann, A study of deformation and strain induced in bulk by the oxide layers formation on a Fe-Cr-Al alloy in high-temperature liquid Pb-Bi eutectic, Acta Mater. 151 (2018) 301–309.
[41] A. Lupinacci, K. Chen, Y. Li, M. Kunz, Z. Jiao, G. Was, M. Abad, A. Minor, P. Hosemann, J. Nucl. Mater. 458 (2015) 70–76.
[42] R. Maaß, S. Van Petegem, D. Grolimund, H. Van Swygenhoven, D. Kiener, G. Dehm, Appl. Phys. Lett. 92 (7) (2008), 071905.
[43] R. Barabash, G. Ice, N. Tamura, B. Valek, J. Bravman, R. Spolenak, J. Patel, J. Appl. Phys. 93 (9) (2003) 5701–5706.
[44] D.N. Ilin, N. Saintier, J.-M. Olive, R. Abgrall, I. Aubert, Int. J. Hydrog. Energy 39 (5) (2014) 2418–2422.